Identifying the Role of the Cationic Geometric Configuration in Spinel Catalysts for Polysulfide Conversion in Sodium-Sulfur Batteries

Chao Yue Zhang[†‡], Xuan Lu[‡], Xu Han[*], Jing Yu[‡\\], Chaoqi Zhang[‡], Chen Huang[‡], Lluís Balcells[§], Alba Garzón Manjón[\\], Jordi Jacas Biendicho[‡], Junshan Li[‡#], Jordi Arbiol[\\⊥], Gengzhi Sun[//], Jin Yuan Zhou[†ǁ*] and Andreu Cabot[‡⊥*]

[†] Key Laboratory for Magnetism and Magnetic Materials of the Ministry of Education & School of Physical Science & Technology, Lanzhou University, Lanzhou, 730000, China.

[‡] Catalonia Institute for Energy Research – IREC, Sant Adrià de Besòs, Barcelona 08930, Spain.

[\\] Catalan Institute of Nanoscience and Nanotechnology (ICN2), Campus UAB, 08193 Bellaterra, Barcelona, Catalonia, Spain.

[§] Institut de Ciència de Materials de Barcelona, ICMAB-CSIC, Campus de la UAB, 08193 Bellaterra, Catalonia, Spain.

[#] Institute of Advanced Study, Chengdu University, Chengdu, 610106 China.

[//] Institute of Advanced Materials, Nanjing Tech University, Nanjing 211816, China.

[⊥] ICREA, Pg. Lluís Companys 23, 08010 Barcelona, Spain.

[ǁ] School of Physics and Electronic Information Engineering Qinghai Normal University, Xining, 810008, China.

KEYWORDS. Sodium polysulfide, sodium-sulfur battery, geometric spinel catalyst, iron cobaltite, cobalt ferrite.

ABSTRACT. The AB_2X_4 spinel structure, with tetrahedral A and octahedral B sites, is a paradigmatic class of catalyst with several possible geometric configurations and numerous applications, including polysulfide conversion in metal-sulfur batteries. Nonetheless, the influence of the geometric configuration and composition on the mechanisms of catalysis, and the precise manner in which spinel catalysts facilitate the conversion of polysulfides remain unknown. To enable controlled exposure of single active configurations, herein, Co^{2+}_{td} and Co^{3+}_{oh} in Co_3O_4 catalysts for sodium polysulfide conversion are in large part replaced by Fe^{2+}_{td} and Fe^{3+}_{oh}, respectively, generating $FeCo_2O_4$ and $CoFe_2O_4$. Through an examination of electrochemical activation energies, the characterization of symmetric cells, and theoretical calculations, we determine that Co^{3+}_{oh} serves as the active site for the breaking of S–S bonds, while Co^{2+}_{td} functions as the active site for the formation of S–Na bonds. The current study underlines the subtle relationship between activity and geometric configurations of spinel catalysts, providing unique insights for the rational development of improved catalysts by optimizing their atomic geometric configuration.

1. INTRODUCTION

Metal-sulfur batteries, specifically sodium-sulfur batteries, are commercially attractive due to the abundance of their active elements, their low-cost potential, and a high theoretical specific capacity of 1675 $mAh \cdot g^{-1}$.[1-4] However, major constraints limit their experimental capacity and cycling stability, hindering their potential for commercialization.[5,6] These constraints include sluggish sulfur reduction reaction (SRR) kinetics, non-uniform deposition of electrically insulating active materials, and shuttling of active species.[7,8]

The incorporation of transition metal-based catalysts into the cathode of metal-sulfur batteries can significantly accelerate sulfur redox reactions, enhancing the capacity, cycling rate, and stability of the battery.[9-12] To rationally optimize the cathode additive material and maximize its catalytic activity, it is critical to understand the involved mechanisms and the contribution of each material parameter. Notwithstanding the significant role played by catalysts in the sulfur redox reaction, the precise mechanisms and structure-property correlations have been poorly investigated. In particular, the impact of the catalyst's geometric configuration on its catalytic activity has been largely overlooked.[13]

Spinels are used as catalysts in a plethora of reactions.[13-17] In a conventional AB_2X_4 spinel, A and B are metals that occupy tetrahedral and octahedral sites, respectively, and X can be O, S, Se, or Te.[18,19] Because charge transfer between cations of different valence states requires a low activation energy, the intrinsic multivalency of spinels dramatically improves its conductivity and catalytic activity.[20,21] The incorporation of these spinels as cathode additive in metal-sulfur batteries have been shown to significantly improve their performance. In our previous work, small amounts of $CoFe_2O_4$ were shown to result in Na-S batteries with unprecedented capacity and cycling stability, particularly under an external magnetic field.[4] Besides, C. Zhang et al. used the $NiCo_2Se_4$ spinel catalyst to exemplify how bimetallic catalysts can improve the specific capacity and

cycle stability of lithium-sulfur batteries.[22] S. Hu et al. used N, F, and B to co-dope $CoFe_2O_{4-x}$ on multi-walled carbon nanotubes to alleviate the "shuttle effect" of lithium-sulfur batteries and improve SRR.[23] Y. Liu et al. demonstrated that $NiCo_2O_4$ can accelerate the catalytic conversion kinetics of soluble intermediate polysulfides by strong chemical interaction, resulting in sulfur cathodes with improved cycle stability.[24] Additionally, D. Luo et al. showed a defective $NiCo_2O_{4-x}$ spinel providing abundant active interfaces and reduced ion diffusion pathways for efficient Li-S reaction.[25]

While the atomic geometric configuration of spinel catalysts significantly impacts overall catalytic behavior, most research in the field has focused on the synergistic "catalytic adsorption" of polysulfides achieved through bimetallic catalysts, without elaborating on the individual contributions of metal atoms in both tetrahedral and octahedral configurations within the material.[26-28] Few previous works have studied the prevailing composition and arrangement of the different elements and their influence on the reaction mechanisms. L. Tian et al. employed multiple metal elements within the tetrahedral gap in the spinel structure and cobalt at the octahedral position to synergistically catalyze the adsorption of lithium polysulfide, which enhanced the electrochemical performance in lithium–sulfur batteries.[29] On the other hand, H. Li et al. showed cooperative catalysis of lithium polysulfides dominated by adsorption competition between metals at different sites of an oxide spinel.[30] To gain a comprehensive understanding of the catalytic behavior, it is crucial to separate the contribution of the tetrahedral and octahedral metal atoms while considering the complete functional unit along with their surrounding coordinated nonmetal atoms.

Since cobalt compounds show high activity toward polysulfide conversion,[1, 10, 31-35] herein, we consider the Co_3O_4 spinel and vary it by introducing catalytically inert Fe to replace either Co^{2+}_{td} or Co^{3+}_{oh} ions.[36, 37] The iron cobaltite $FeCo_2O_4$ and cobalt ferrite $CoFe_2O_4$ obtained expose larger ratios of either Co^{3+}_{oh} or Co^{2+}_{td} within monotype geometric units. With this separate passivation strategy, we aim at identifying the role of each cobalt ion in the polysulfide reaction. Using the Arrhenius equation, the activation energy for sodium polysulfide reduction is determined and Co^{3+}_{oh} is identified as the active site promoting the dissociation of nonpolar polysulfide bonds (S–S*). Conversely, Co^{2+}_{td} is identified as the active site promoting the polysulfide polar bond (S–Na*). Theoretical calculations reveal the synergy between the central metal site and the coordinating non–metal sites in each geometric configuration that leads to a faster SRR.

2. RESULTS AND DISCUSSION

2.1 Spinel structural, chemical, and magnetic properties.

Spinel oxide nanoparticles, both unsupported and supported on carbon nanofibers (CNFs), were produced using a hydrothermal method (see the Experimental Section in the Supporting Information, SI, for details). To investigate the role of Co^{2+}_{td} and Co^{3+}_{oh} in spinel Co_3O_4 towards polysulfide conversion, we deactivate Co^{2+} and Co^{3+} in their corresponding tetrahedral and octahedral geometries by replacing them with catalytically inert Fe^{2+} and Fe^{3+}, respectively (Figure 1a). With this aim, we produced $FeCo_2O_4$ and $CoFe_2O_4$ particles using the same hydrothermal method but replacing part of the Co with Fe ions. In the process of material synthesis, Co^{2+} and Fe^{3+} (with a ratio Co/Fe=0.5) were used as precursors for the synthesis of $CoFe_2O_4$, and Fe^{2+} and Co^{3+} (with a ratio Co/Fe=2) as the precursors for the synthesis of $FeCo_2O_4$. Thus, not mediating any redox between ions, Co^{2+} ions should occupy the tetrahedral positions in $CoFe_2O_4$ and Co^{3+} should occupy the octahedral sites in $FeCo_2O_4$.[38,39] In addition, as reference material, we also prepared Fe_3O_4 nanoparticles supported on CNFs (Figures S1 and S2).

Scanning electron microscopy (SEM), inductively coupled plasma-optical emission spectroscopy (ICP-OES), high–resolution transmission electron microscopy (HRTEM), and atomic resolution aberration-corrected (AC) high angle annular dark field (HAADF) scanning transmission electron microscopy (STEM) images as well as electron energy loss spectroscopy (EELS) compositional maps of the parent Co_3O_4 and the Fe-substituted materials, $FeCo_2O_4$ and $CoFe_2O_4$, are displayed in Figures S2-S10. Electron microscopy characterization shows the Co_3O_4, $FeCo_2O_4$, and $CoFe_2O_4$ particles to have faceted morphologies and an average size in the range of 11-16 nm (Figure S11). The $FeCo_2O_4$ and $CoFe_2O_4$ particles were slightly smaller than Co_3O_4 and no significant difference in shape among the different materials was identified.

The fast Fourier transform (FFT) generated from atomic resolution AC HAADF STEM images (Figures 1c and 1d) and HRTEM images (Figures S5, S7, and S9) show the same three sets of lattice fringes for all the materials, assigned to interplanar spacings that match the (3 –1 1), (3 1 –1), and (0 2 –2) planes of the Co_3O_4, $CoFe_2O_4$, and $FeCo_2O_4$ spinels, confirming the targeted crystal structure.[18] The powder X–ray diffraction (XRD) patterns of Co_3O_4, $CoFe_2O_4$, and $FeCo_2O_4$ (Figure 1b) display the fingerprint of the spinel structure with sharp characteristic peaks at 2θ = 31, 37, 45, 57, 59, and 65° that can be assigned to the (2 2 0), (3 1 1), (4 0 0), (4 2 2), (5 1 1) and (4 4 0) family planes of the cubic spinel (Fd–3m). No additional XRD peaks were detected, confirming the pure–phase spinel structure.[40]

Within the AB_2O_4 spinel, Co^{2+} ions tend to occupy the tetrahedral sites and Co^{3+} ions the octahedral (Figures S12 and S13).[41-46] A first attempt to determine the location of Co ions in $CoFe_2O_4$ and $FeCo_2O_4$ was made by correlating experimental and theoretical data of the materials' magnetic properties (See details in the Experimental Section on the SI). Figure S14a displays the theoretical magnetic moments of each configuration calculated using density functional theory (DFT) and Figure S14b shows the magnetic hysteresis loops of the different materials measured at ambient temperature. In $CoFe_2O_4$, assuming that Co ions occupy octahedral positions, the calculated magnetic moment is 0 μB, which does not agree with the strong magnetic moment measured for this sample. Therefore, in $CoFe_2O_4$, the probability of Co ions occupying tetrahedrons is greater than that of octahedrons. On the other hand, when assuming that half of the available cobalt atoms occupy tetrahedral positions and the other half occupy octahedral positions in $FeCo_2O_4$, DFT calculations anticipate the material to be antiferromagnetic, which is also inconsistent with the experimental data (Figure S14b). Thus, in $FeCo_2O_4$, the probability of Co ions occupying octahedrons is greater than that of tetrahedrons.

The valence state of cobalt in Co_3O_4, $CoFe_2O_4$, and $FeCo_2O_4$ was investigated using X–ray photoelectron spectroscopy (XPS, Figure 1f and S15).[47-52] Co 2p XPS spectra display two doublets associated with two Co chemical environments, Co^{3+} at 779.7 eV (Co $2p_{3/2}$) and Co^{2+} at 781.6 eV (Co $2p_{3/2}$), and two additional satellite peaks. Notice that the different satellite peak areas of the three materials correlate well with their different

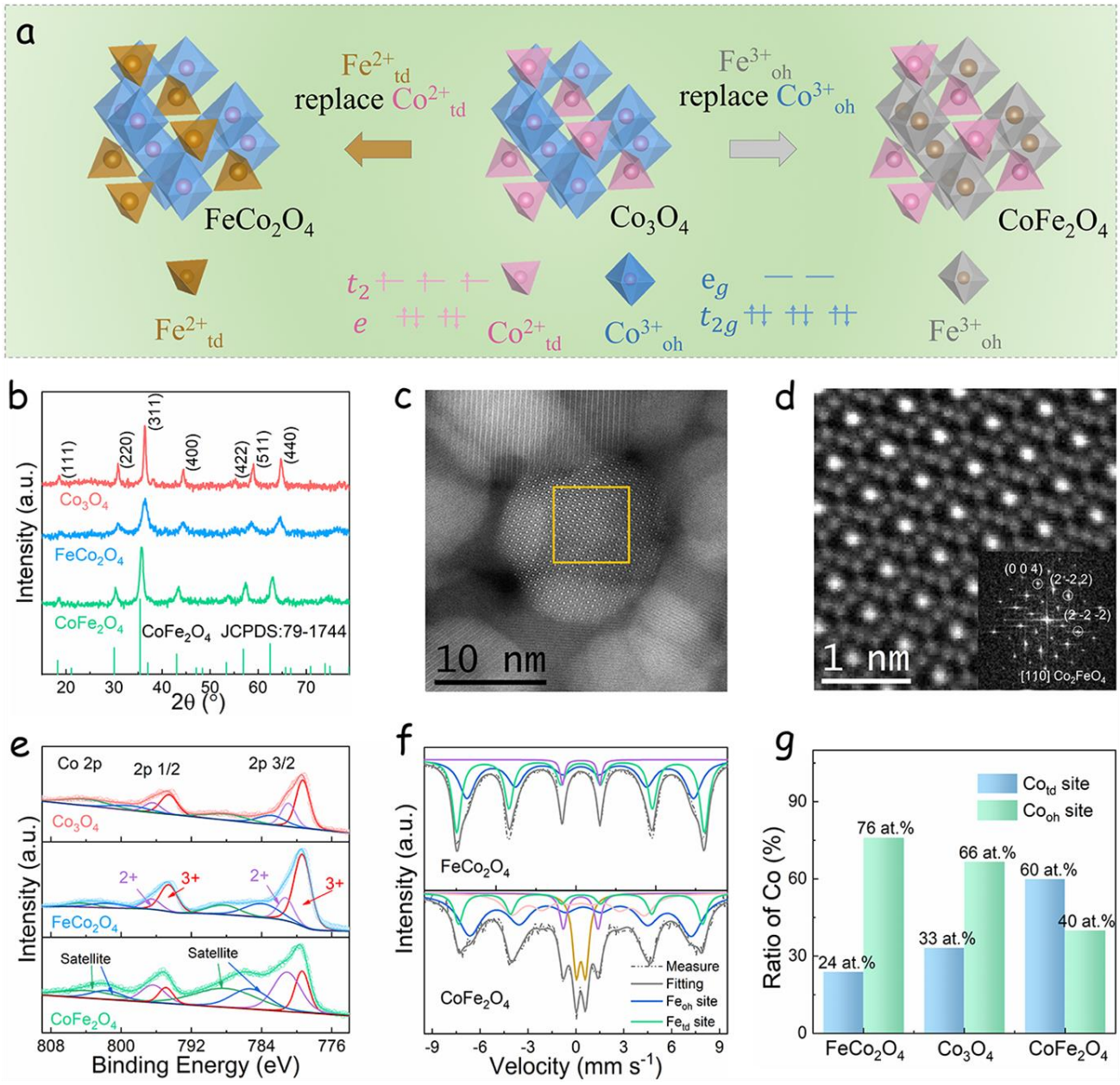

Figure 1. (a) Schematic illustration of spinel structures of Co_3O_4, $CoFe_2O_4$, and $FeCo_2O_4$. (b) XRD patterns of Co_3O_4, $CoFe_2O_4$, and $FeCo_2O_4$. (c) Atomic resolution AC HAADF STEM of $FeCo_2O_4$ nanoparticles. (d) Power spectrum of this image and detail of the orange squared region from (c). (e) XPS spectra of Co 2p for Co_3O_4, $CoFe_2O_4$, and $FeCo_2O_4$. (f) Mössbauer spectra of $FeCo_2O_4$ (upper) and $CoFe_2O_4$ (down) at room temperature. (g) Ratio of tetrahedral and octahedral Co site in $FeCo_2O_4$ and $CoFe_2O_4$.

magnetization.[53,54] The area ratio of Co^{3+}/Co^{2+} was used to estimate the occupancy of Co in the octahedral or tetrahedral sites.[55] As shown in Table S1, the $Co^{3+}/(Co^{2+}+Co^{3+})$ ratio within Co_3O_4 was 63%, implying that 2/3 of Co^{3+} is in octahedral sites and 1/3 in tetrahedral sites. Notably, in $CoFe_2O_4$, ca. 64.5% of Co ions were found in a Co^{2+} chemical environment, i.e. occupying tetrahedral sites, while in $FeCo_2O_4$, 76.9% of Co ions were found as Co^{3+}, i.e. occupying octahedral sites.

Additional insight into the site occupation of Co within the spinel structure was inferred from the site occupation of Fe determined using Mössbauer spectroscopy.[56] The room temperature Mössbauer spectra of $FeCo_2O_4$ and $CoFe_2O_4$ are shown in Figure 1f and the fitted hyperfine parameters are listed in Table S2. Both spectra require at least two sextets to be properly fitted, showing that in both samples Fe ions occupy tetrahedral and octahedral sites.[57] Fe ions occupying the tetrahedron have associated the sextet state with the smaller hyperfine magnetic field around 44 T, while Fe ions on the octahedron are assigned to the sextet with the maximum hyperfine magnetic field around 48 T state. The presence of an intermediate doublet with zero hyperfine field in the $CoFe_2O_4$ is related to the emergence of a paramagnetic phase related to small ferrite crystal domains.[56] Besides, in $CoFe_2O_4$, a sextet related to an amorphous phase is also introduced (pink line).[53] As shown in Table S2 and Figure 1g, from the fitting of the Mössbauer spectra, in $FeCo_2O_4$ the Fe_{td} occupation is 54 at.% and the Fe_{oh} occupation is around 48 at.%. In $CoFe_2O_4$, the Fe_{td} occupation is around 20 at.% and that of Fe_{oh} is around 80 at.%.

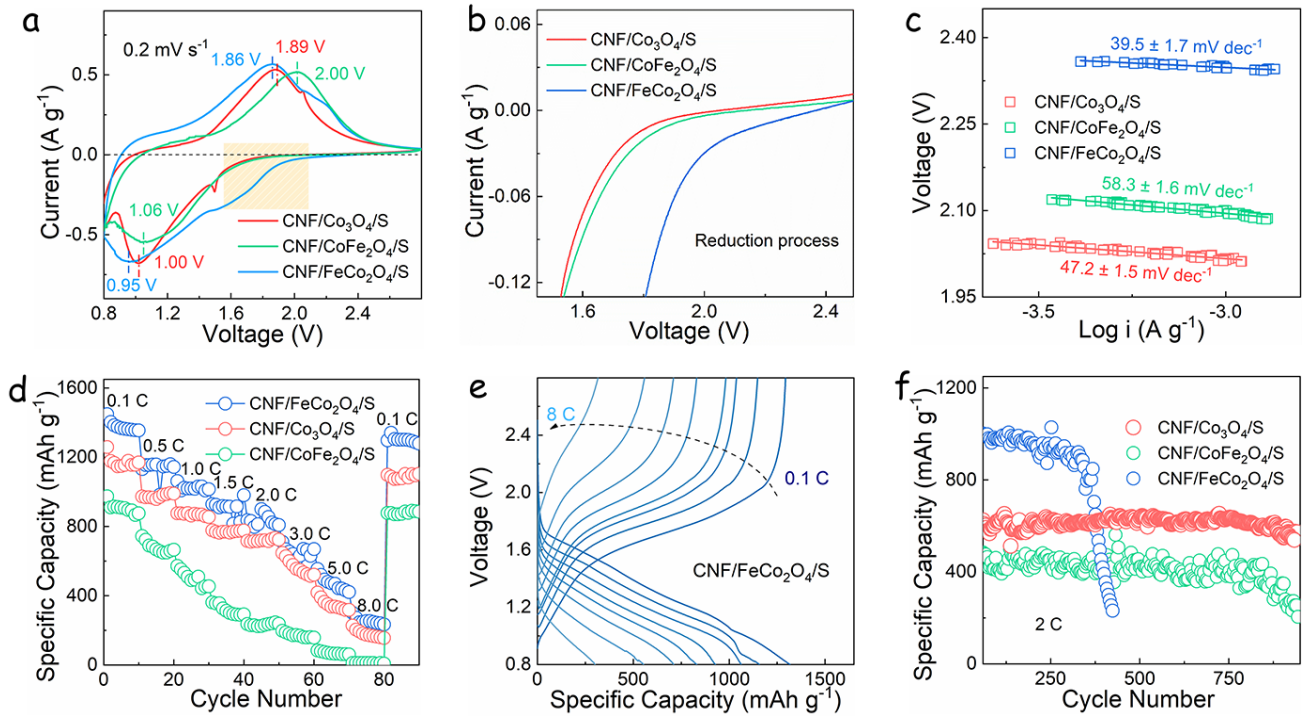

Figure 2. Electrochemical performance of CNF/Co_3O_4/S, CNF/$CoFe_2O_4$/S and CNF/$FeCo_2O_4$/S electrodes in half cells: (a) CV curves. (b) LSV curves from 2.41 V to 1.58 V obtained from Figure 2a yellow region. (c) Tafel plots. (d) Rate performance; (e) Charge and discharge curves of CNF/$FeCo_2O_4$/S at different current densities. (f) Long term cycling performance at 2 C.

From EDX and ICP data (Figures S3 and S4), the ratio of Co and Fe is 2:1 in $FeCo_2O_4$ and 1:2 in $CoFe_2O_4$. Thus, we estimate that there are 76 at.% Co in octahedral site on $FeCo_2O_4$ and 60 at.% Co in tetrahedral site on $CoFe_2O_4$ (Figure 1g). Hence, Mössbauer spectroscopy confirms that in $CoFe_2O_4$ and $FeCo_2O_4$, Co is mainly distributed in tetrahedral and octahedral positions, respectively. These results are consistent with XPS data, pointing at a similar site occupation at the core and the surface of the particles. Overall, according to the Mössbauer spectroscopy, the formula of the three materials, $FeCo_2O_4$, $CoFe_2O_4$, and Co_3O_4, can be written as: $(Fe_{0.52}Co_{0.48})_{td}(Fe_{0.48}Co_{1.52})_{oh}O_4$, $(Fe_{0.40}Co_{0.60})_{td}(Fe_{1.6}Co_{0.40})_{oh}O_4$, and $(Co_{0.33})_{td}(Co_{0.66})_{oh}O_4$. However, to simplify nomenclature, we will continue using $FeCo_2O_4$, $CoFe_2O_4$, and Co_3O_4 from here on.

Raman spectroscopy was used to gain further insight into each ion location.[58] The Raman spectrum of a spinel oxide displays two sets of peaks, A_{1g} and T_{1g}, that are ascribed to specific vibrational modes of the tetrahedrons and octahedrons, respectively (Figure S16). Compared with the Raman spectrum of Co_3O_4, the A_{1g} modes of the $FeCo_2O_4$ spectra and the T_{1g} modes of $CoFe_2O_4$ significantly redshift to lower energies, while the position of the T_{1g} modes of $CoFe_2O_4$ and the A_{1g} modes of $FeCo_2O_4$ remain unaltered. This implies the introduction of Fe to strain the metal-oxygen bond mainly in the tetrahedrons for $FeCo_2O_4$ and mainly on the octahedrons for $CoFe_2O_4$, which is consistent with Co being mainly located in octahedral sites in $FeCo_2O_4$ and tetrahedral sites in $CoFe_2O_4$.[32]

According to the literature, the tetrahedrally and octahedrally occupied Co ions in Co_3O_4 prefer the electronic configurations of Co^{2+} ($e^4t_2^3$) and Co^{3+} ($t_{2g}^6e_g^0$), respectively.[59] As shown in Figure S17, the lower Co orbitals such as e and t_{2g} orbitals are fully occupied and cannot participate in bonding. In terms of polysulfide conversion, what truly counts is the interaction between the higher Co d–orbitals (i.e. t_2 and e_g) and the S p–orbitals (p_x, p_y, and p_z). During the polysulfide conversion, along with the breakdown of the nonpolar S–S and the formation of the polar S–Na bonds, the interaction and electronic coordination defining the creation of the new bonds also play an important role, as discussed below.

2.2 SRR electrochemistry performance on Co^{3+}_{oh} and Co^{2+}_{td} sites

To study the SRR electrocatalytic effect of different Co sites in the spinel structure, CNF/Co_3O_4, CNF/$CoFe_2O_4$, and CNF/$FeCo_2O_4$ were loaded with sulfur at around 52-56 wt.% (Figure S18). The corresponding electrodes are denoted as CNF/Co_3O_4/S, CNF/$CoFe_2O_4$/S, and CNF/$FeCo_2O_4$/S. Cyclic voltammetry (CV) measurements were performed between 0.8 and 2.8 V at a scan rate of 0.2 mV s^{-1} (Figure 2a). To exclude a potential role of Fe in the sulfur reduction reaction, the CNF/Fe_3O_4/S electrode was also tested as a reference (Figure S19). During the first discharge curve (Figure S20), the pristine loaded sulfur is reduced to sodium sulfide:

$$S_8 \rightarrow Na_2S \quad (1)$$

When charging, the anodic peak at ca. 2.0 V corresponds to the transformation of Na_2S to Na_2S_x (x = 4 and 6).[2, 60] In the next redox processes (Figure 2a), the reaction goes back and forth between Na_2S and Na_2S_x, without full oxidation to S_8 in this voltage range (2):[61]

$$Na_2S \leftrightarrow Na_2S_2 \leftrightarrow Na_2S_x \quad 1.2\text{-}2.4 \text{ V vs } Na^+/Na \quad (2)$$

As described in the literature,[61] in the cathodic scans, the reduction of sulfur species is proposed to follow several steps:

$$Na_2S_x \rightarrow Na_2S_4 \quad 2.8\text{-}1.6 \text{ V vs } Na^+/Na \quad (3)$$

$$Na_2S_4 \rightarrow Na_2S_2/Na_2S \quad 1.6\text{-}1.3 \text{ V vs } Na^+/Na \quad (4)$$

$$Na_2S_2 \rightarrow Na_2S \qquad 1.3\text{-}0.8 \text{ V vs } Na^+/Na \qquad (5)$$

when the battery discharges to 1.6 V, Na_2S_x is converted into Na_2S_4 (3); and when discharged to 1.3 V, polysulfides begin to convert to Na_2S_2 and Na_2S (4). When finally discharged to 0.8 V, there is a complete conversion into Na_2S (5). In the anodic scan, the reverse reactions take place in the voltage range of 1.5 to 2.4 V. Depending on the overlap between the three reaction processes, three, two, or just one reduction and oxidation peaks are experimentally observed.[4, 61-63]

The CNF/$FeCo_2O_4$/S electrode exhibits two clearly differentiated reduction and oxidation peaks, with the lowest reduction peak potential at 0.95 V (Figure 2a) and the highest reduction onset potential at 2.01 V (Figure 2b). In contrast, the CNF/$CoFe_2O_4$/S electrode shows a larger overlap of the reduction and oxidation processes, with just one clear maximum at 1.06 V. This difference could be attributed to $FeCo_2O_4$'s greater catalytic ability for sodium polysulfide transformation, whereas the $CoFe_2O_4$-based electrode with the highest reduction potential peak has the fastest sodium sulfide conversion kinetics (Figure 2a). On the other hand, the CNF/Co_3O_4/S electrode shows a broad band and a narrow peak both in the forward and reverse scans. The narrow peak must be related to the SRR process, as previously reported,[4, 63] since it cannot be observed in the CV of the CNF/Co_3O_4 electrode without sulfur (Figure S21). Actually, without sulfur, there is no redox peak in the CV of CNF/Co_3O_4, pointing to a high stability of the electrode material during cycling. On the other hand, the CV curves of the CNF/Fe_3O_4/S electrode displayed a very low sulfur redox peak, implying a very moderate sulfur redox kinetics (Figure S19).

Figure 2b shows the linear sweep voltammetry (LSV) curves of the different electrodes from 2.41 V to 1.58 V obtained from the Figure 2a yellow region. CNF/Co_3O_4/S and CNF/$CoFe_2O_4$/S display very similar LSV curves, with similar overpotentials. On the other hand, the CNF/$FeCo_2O_4$/S electrode shows a much higher overpotential for the initial discharge process, which is consistent with Co_{oh} having a key role in accelerating the conversion of the polysulfides.

Figure 2c shows the Tafel plots obtained from the reduction process in the LSV curves. The Tafel slope was calculated from a narrow voltage interval around the zero current voltage to prevent mass transfer limitation.[1] The Tafel slope of the CNF/$FeCo_2O_4$/S cathodic reduction process was estimated at 40 ± 2 mV dec^{-1}, which was lower than in CNF/Co_3O_4/S (47 ± 2 mV dec^{-1}) and CNF/$CoFe_2O_4$/S (58 ± 2 mV dec^{-1}). The above results point to Co^{3+}_{oh} as the main contributor to the conversion of the initial polysulfides while Co^{2+}_{td} contributes to accelerating the subsequent sulfur conversion reactions.

While Co_3O_4 contains the largest density of Co_{oh} and Co_{td} sites, its performance towards the conversion of polysulfides and sodium sulfide is lower than that of $FeCo_2O_4$ and $CoFe_2O_4$. Thus, while we see Fe sites to be inactive (Figure S19), the inserted Fe seems to influence the activity of both tetrahedral and octahedral Co sites potentially by changing the bonding state and electronic structure of adjacent Co atoms. According to the classical catalysis theory, when increasing the bond distance, the d-band center moves up closer to the Fermi level, and the catalytic performance should be improved.[51, 64, 65] To determine the influence of Fe, the bond length of the three materials was calculated using DFT (Figure S22). DFT results show the bond length of the tetrahedron Co-O_4 of $CoFe_2O_4$ (1.92 Å) and the octahedron Co-O_6 $FeCo_2O_4$ (1.95 Å) to be higher than in Co_3O_4 (1.88 and 1.92 Å respectively). Thus, not considering the geometric configuration, the increase of the Co-$O_{4/6}$ distance related to the presence of Fe also contributes to improving the catalytic performance of Co both in $CoFe_2O_4$ and $FeCo_2O_4$ compared with Co within Co_3O_4.

As shown in Figures 2d,e and S23 and S24, the CNF/$FeCo_2O_4$/S electrode exhibits 1421, 1134, 1060, 920, 822, 710, 548, and 293 mA h g^{-1} discharge specific capacities at 0.1, 0.5, 1.0, 1.5, 2.0, 3.0, 5.0 and 8.0 C (1 C = 1675 mA g^{-1}) respectively, which are significantly higher than those obtained from CNF/Co_3O_4/S and CNF/$CoFe_2O_4$/S electrodes. When the current density was switched back to 0.1 C, a high discharge specific capacity of 1297 mA h g^{-1} was recovered. Despite its high capacity, the CNF/$FeCo_2O_4$/S electrode experiences poor cycle stability, with a sharp drop in capacity after 350 cycles (Figures 2f and S25). As observed by SEM-EDX analysis of the cycled material (Figures S25 and S26), after 350 cycles the failed CNF/$FeCo_2O_4$ electrode exhibits uneven sodium sulfide deposition and side reactions within the electrolyte.[62] On the other hand, CNF/Co_3O_4/S exhibits a capacity fade of just 0.015% per cycle during 1000 cycles at 2.0 C with stable coulombic efficiency. Besides, although the capacity of the CNF/$CoFe_2O_4$/S electrode is lower, its cycle stability is significantly higher than that of the CNF/$FeCo_2O_4$ electrode. These electrochemical results further suggest that Co^{3+}_{oh} and Co^{2+}_{td} relate with the ability to convert longer and shorter polysulfides respectively.

2.3 Polysulfides catalytic ability on Co^{3+}_{oh} and Co^{2+}_{td} sites

The polysulfide conversion kinetics was further assessed using symmetric cells assembled using two identical CNF/spinel electrodes combined with long-chain sodium polysulfides, glass fibers as a separator, and dimethyl carbonate (DMC)/ethylene carbonate (EC) (1:1) with 5 wt.% fluoroethylene carbonate (FEC) as electrolyte (see the SI for details). Figure 3a shows the measured charge and discharge potentials of a reference CNF/polysulfide cell tested at 1 mA cm^{-2}. Increasing the number of cycles, the deposition of short–chain sulfides increases the electrical resistance and thus the overpotential.[66] The electrodes were characterized using SEM-EDX at different stages of deposition: I as the initial deposition stage; II as the middle stage of deposition; and III as the final deposition stage (Figures S27). At stage I, the polysulfides are dispersed. As the deposition progresses, spherical sodium sulfide particles start to form on the CNFs and coexist with dispersed polysulfides, as seen in stage II. At stage III, after one hour of deposition, the dispersed polysulfides have completely converted into spherical sodium sulfide. Due to the symmetry of the electrode, when the working electrode undergoes the nucleation reaction of sodium sulfide, the counter electrode is undergoing the dissolution of sodium sulfides (Figure S28, III stage).

Taking classical nucleation theory as a starting point, it is commonly acknowledged that the nucleation of a new solid phase depends on the free energy barrier and the thermodynamic costs of forming critical atomic clusters.[67, 68] For electrodeposition, this nucleation barrier can be effectively tuned by changing the electrochemical supersaturation at the working electrode by tuning the overpotential of the reduction reaction (Figure 3b). Traditionally, the driving forces of the electrocrystallization process can be divided into reaction overpotential, charge transfer overpotential, diffusion overpotential, and crystallization overpotential.[67, 69] However, since it is difficult to identify each source of electrode polarization, we just differentiate two characteristic

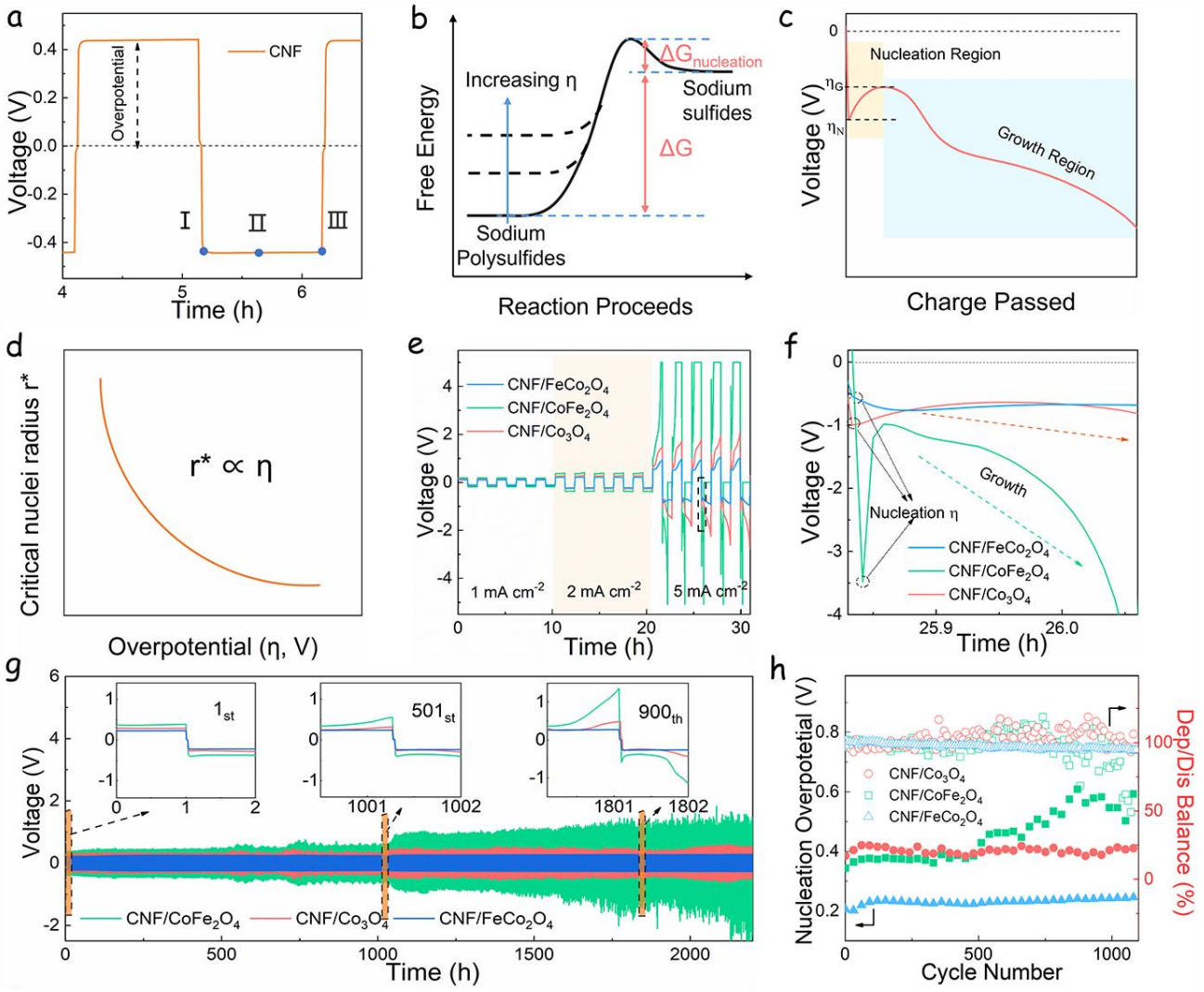

Figure 3. (a) Constant current charge and discharge of CNF/polysulfide//CNF/polysulfide symmetric cells at 1 mA cm^{-2}. (b) Free energy schematic showing the effect of increasing the overpotential on the nucleation barrier. (c) Schematic diagram comparing typical voltage curves for galvanostatic sodium sulfide deposition. (d) Schematic plot of the dependence of critical sodium sulfide nuclei radius on the overpotential of sodium sulfide deposition. (e) Rate capability of the polysulfide//polysulfide symmetric cells with CNF/Co_3O_4, CNF/$CoFe_2O_4$, and CNF/$FeCo_2O_4$ electrodes. (f) Expanded area of the discharge process of 5 mA cm^{-2} from (e). (g) Cycle stability of symmetric cells. (h) Statistics on nucleation voltage and deposition/dissolution (dep/dis) potential balance.

overpotentials observed during galvanostatic sodium sulfide electrodeposition: (1) the nucleation overpotential (η_N) measured as the magnitude of the voltage spike at the onset of sodium sulfide deposition; and (2) the growth overpotential (η_G) observed after nucleation occurs and sodium sulfide continues to grow (Figure 3c). As the galvanostatic sodium sulfide electrocrystallization process occurs at variable supersaturation,[70] η_N and η_G are useful for their ease of extraction from experimental data and their correlation with important parameters. At the beginning of the galvanostatic sodium sulfide deposition process, the potential of the working electrode drops below 0 V, where the electrochemical overpotential is sufficient to drive the nucleation of sodium sulfide nuclei. After initial nucleation occurs, the overpotential rises to $-\eta_G$, which remains negative compared to the counter electrode, and sodium sulfide nuclei continue to grow due to the lower electrode polarization for sodium sulfide growth compared to the nucleation step.

The classical equation of uniform nucleation can be simply used to understand the dependence of electrodeposited sodium sulfide core size on electrodeposition overpotential and applied current density.[70, 71] The Gibbs energy ($\Delta G_{nucleation}$) required to form a spherical nucleus of radius r depends on the bulk and surface free energies:[68]

$$\Delta G_{nucleation} = -\frac{4}{3}\pi r^3 \Delta G_V + 4\pi r^2 \gamma \quad (6)$$

where ΔG_V is the change in free energy per unit volume and γ is the surface energy of the polysulfide-electrolyte interface. The relationship between deposition overpotential η and ΔG_V is:

$$\Delta G_V = \frac{F|\eta|}{V_m} \quad (7)$$

here F is Faraday's constant and V_m is the molar volume of sodium sulfide. Therefore, the critical radius is as follows:[67, 71]

$$r_{crit} = \frac{2\gamma V_m}{F|\eta|} \quad (8)$$

For heterogeneous nucleation, such as sodium sulfide deposited on the electrode surface, the energy barrier to form critical nuclei is lowered, but the expression of the critical nuclei size is the same as in Equation 8. To investigate the nucleation process, symmetric cells with CNF/polysulfides electrodes were charged and discharged at constant current density (of 1 mA cm^{-2}, 2 mA cm^{-2}, or 5 mA cm^{-2}) with 2 h cycles (Figure S29). The obtained data show an inverse relationship between the sodium sulfide nuclei size and the overpotential (Figures 3d and S30).

In the symmetric cells assembled using CNF/Co_3O_4/polysulfide, CNF/$CoFe_2O_4$/polysulfide, and CNF/$FeCo_2O_4$/polysulfide electrodes, increasing the current density resulted in wider deposition overpotentials (Figure 3e). Among the three different electrodes, CNF/$FeCo_2O_4$/polysulfide exhibited the smallest overpotential, while CNF/$CoFe_2O_4$/polysulfide showed the largest, indicating that Co^{3+}_{oh} is more effective in transforming long–chain sodium polysulfides into short–chain sulfides than Co^{2+}_{td}.

Besides, a different evolution of the nucleation voltages was observed in the three electrodes as the deposition current density increased (Figure 3f). According to equations 6 and 7, larger η caused larger ΔG_V and thus larger $\Delta G_{nucleation}$. The CNF/$FeCo_2O_4$/polysulfide electrode exhibited the lowest nucleation voltage, indicating that Co^{3+}_{oh} has associated the lowest energy barrier for the nucleation of sodium sulfides.[72]

The cycling stability of the sodium sulfide nucleation-dissolution process, measured on the symmetric cells at a current density of 2 mA cm^{-2}, is displayed in Figure 3g. During the initial deposition of sodium sulfide, the cell shows a relatively low overpotential. However, as the deposition and dissolution cycling continued, the overpotentials of CNF/Co_3O_4 and especially CNF/$CoFe_2O_4$ gradually increased, while the CNF/$FeCo_2O_4$ electrodes maintained low energy barriers. The insets in Figure 3g show the detailed changes in overpotential at the 1st, 501st, and 900th cycles.

After over 2000 hours of cycling, i.e. over 1000 cycles, the morphology of the three electrodes at stage III of the deposition process was examined (Figure S31). The CNF/$FeCo_2O_4$ electrode exhibited spherical sodium sulfide particles with a significantly larger radius than CNF/Co_3O_4 and especially CNF/$CoFe_2O_4$. The nucleation overpotential and deposition/dissolution balance (deposition potential / dissolution potential × 100) during long cycling are presented in Figure 3h. As cycling progressed, CNF/$FeCo_2O_4$ exhibited a stable η_N and near 100% deposition/dissolution balance, while CNF/ $CoFe_2O_4$ and CNF/Co_3O_4 shows more unbalance deposition/dissolution ability, indicating that Co^{3+}_{oh} has a far better ability to convert polysulfides than Co^{2+}_{td}. The optical photographs of the polysulfide solution with $FeCo_2O_4$, $CoFe_2O_4$ and Co_3O_4 are shown in Figure S32. The $FeCo_2O_4$ vial has the clearest solution indicating the best polysulfide adsorption ability that is associated with the presence of Co^{3+}_{oh}.

To investigate the kinetics of conversion of long–chain polysulfides to short–chain sodium sulfide, electrochemical impedance spectroscopy (EIS) measurements were performed on CNF/Co_3O_4/S, CNF/$CoFe_2O_4$/S, and CNF/$FeCo_2O_4$/S electrodes at temperatures of 300 K, 315 K and 330 K (Figures 3a, S33–36, Table S3 and S4). EIS data were fitted using the equivalent circuit presented in Figure 4a.[2, 73-75] Within the model circuit, the CR element CPE_{Surf}-R_{surf} accounts for the deposition of adsorbed sodium polysulfide on the electrode surface and provides the first semicircle in the Nyquist plot of the EIS spectrum. The CR element CPE_{ct}-R_{ct} corresponds to the charge transfer process during polysulfide conversion and provides a second semicircle in the EIS spectrum. The "tail" in the EIS spectrum provides from the ion transfer resistance of the cell and it is taken into account using the Warburg resistance.[76] The intercept of the first semicircle with the horizontal axis at the highest frequency corresponds to the internal resistance (R_s) of the battery, including the resistance of electrodes and the electrolyte.[77] CPE_{surf} and CPE_{ct} are constant phase elements from surface deposition and charge transfer, respectively.[78] The activation energy (E_a) for the charge transfer process associated with the polysulfide conversion was estimated for each voltage by fitting the R_{ct} values obtained at different temperatures with an Arrhenius equation.[78, 79] Figure 3c shows that during the SRR, at 2.3 V and 1.8 V, the E_a of the CNF/$FeCo_2O_4$/S electrode was 0.24 and 0.26 eV, respectively. These values are smaller than those obtained for CNF/Co_3O_4 and especially CNF/$CoFe_2O_4$ (Figure 4c, Table S3). These results indicate that Co^{3+}_{oh} has a lower potential barrier for the early Na_2S_x (x = 5–8) to Na_2S_x (x = 3–5) conversion than Co^{2+}_{td}. This is consistent with the lowest nucleation energy required for the conversion of polysulfides measured in the symmetric cell. However, when the SRR process continues, at 1.3 V and 0.8 V, the lowest E_a values were obtained for the CNF/$CoFe_2O_4$/S electrode at 0.30 and 0.33 eV, respectively. These results confirm that Co^{3+}_{oh} is particularly effective in promoting the conversion of Na_2S_x (x = 5–8) to Na_2S_2, whereas Co^{2+}_{td} is more effective in converting Na_2S_2 to the final Na_2S.

SRR thermodynamics on Co^{2+}_{td} and Co^{3+}_{oh}, were determined using DFT calculations of the Gibbs free energy (Figure 4d and S37–S40, see SI for additional details).[5, 6] Due to the large size of S_8 and sodium polysulfides, the reduction of S_8 and Na_2S_6 by Co^{3+}_{oh} and Co^{2+}_{td} on the Co_3O_4 surface may affect each other, so they are combined and discussed first. S_8 ring molecules spontaneously react with Na ions to form Na_2S_6. As the reaction proceeds, the energy required for the transformation of Na_2S_6 into Na_2S_2 at Co_3O_4–Co^{3+}_{oh} and $FeCo_2O_4$–Co^{3+}_{oh} sites are 0.97 and 0.79 eV, respectively. These values are lower than those obtained for Co_3O_4–Co^{2+}_{td} and $FeCo_2O_4$–Co^{2+}_{td} sites (1.46 and 2.55 eV, respectively). In the above process of conversion of active species, sulfur–sulfur bonds are broken to release energy. Thus, the lower energies required by Co^{3+}_{oh} are consistent with the higher ability of this ion to cleave these sulfur–sulfur bonds. In contrast, the solid conversion of Na_2S_2 into Na_2S just involves the formation of a sulfur–sodium bond. In the process of solid-solid conversion, due to their solid state, their arrangement is much more orderly than that of polysulfide molecules.[80] For the conversion process of Na_2S_2 to Na_2S, we can consider that it is due to the intercalation of sodium ions into the lattice of Na_2S_2 to form new Na-S bonds and then transform to Na_2S (Figure S41). In this process, the energies required for Co_3O_4–Co^{2+}_{td} and $FeCo_2O_4$–Co^{2+}_{td} are –0.21 and –2.69 eV, well below those of Co_3O_4–Co^{3+}_{oh} and $FeCo_2O_4$–Co^{3+}_{oh} sites, consistent with the higher ability of Co^{2+}_{td} in formation S–Na bonds. Overall, the energy distribution analysis shows that Co^{3+}_{oh} is more favorable for breaking sulfur–sulfur bonds during the conversion of long–chain polysulfides to short–chain polysulfides, while Co^{2+}_{td} is more effective at the formation of sulfur–sodium bonds during the final conversion of Na_2S_2 to Na_2S. These findings suggest that both Co^{3+}_{oh} and Co^{2+}_{td} play important roles in the SRR process, and their relative contributions depend on the specific reaction stage. The energy barrier for each reaction pathway is influenced by various factors such as the local environment and the nature of the

active site, which should be considered for the design and optimization of high–performance sulfur electrodes for advanced energy storage applications.

2.4 Theoretical analysis of polysulfides and sulfides with Co^{3+}_{oh} and Co^{2+}_{td} sites

To elucidate the source of the SRR activity observed in Co^{3+}_{oh} and Co^{2+}_{td}, we investigated the interaction between the d–band structure of cobalt and the bonds involving sulfur and sodium using DFT calculations. Estimates of the spin–orbit coupling of Na–S* (number of band electrons, Nb = 5) and S–S* (Nb = 6) interactions are shown in Figure 5a and Figure S42-S45 for Co^{3+}_{oh} and Co^{2+}_{td}, respectively.[30, 81] Na–S* and S–S* of active substances react in the y direction, Co^{3+}_{oh} half–filled d_{x2-y2}, d_{xy}, d_{yz} orbitals point to S–S* by re–bonding, covalent Co^{3+}_{td}–S–S* bond as an intermediate. According to Hund's rule, a lower number of d electrons in the cation, such as Co^{3+}_{oh} (Nd = 5) (Figure 5a), results in lower d–band center positions and occupancy of the partially filled new interaction bond between S–S* and Co^{3+}_{oh} site, whereby the newly formed antibonding state has higher energy that makes S–S* unstable on Co^{3+}_{oh} for easier decomposition. Similarly, as shown in Figure S43, when S–S* is on Co^{2+}_{td}, the electronic filling rules after rebounding make the π* orbitals in a half-full state. Compared with Co^{3+}_{oh}, this state is more stable, and S–S* adsorbed on Co^{2+}_{td} is less likely to decompose. This causes Co^{3+}_{oh} to have an advantage over Co^{2+}_{td} in promoting the transformation of S_8 to Na_2S_2 in the S–S bond. However, when Na_2S_2 is converted to Na_2S, the determining conversion reaction changes from cleaving S–S* to forming Na–S* (Figure S41), and the polarity of Na–S* is stronger and Nb = 5. When forming a bond, the bonding orbital of Na–S*on Co^{3+}_{oh} is full. Obviously, the orbital of Na–S* bonding on Co^{2+}_{td} is at a higher energy level (Figure S44), thus Na–S* is easier to form at its site. To verify this assumption, the partial density of states (PDOS) of the S–S* bond and Na–S* bond adsorbed on Co^{3+}_{oh} and Co^{2+}_{td}, respectively, are displayed in Figures S46 and S47. The antibonding center π* between Co^{3+}_{oh} and S–S* is greater (2.83 eV) than that between Co^{2+}_{td} and S–S* (2.26 eV). Conversely, the bonding center π between Co^{2+}_{td} and S–Na* is smaller (-1.47 eV) than that between Co^{3+}oh and S–Na* (-1.39 eV), indicating the Na–S* bond is easily formed on the Co^{2+}_{td} sites. The PDOS results validate the hypothesis proposed in Figures 5a, S43, and S44.

Additionally, the calculated adsorption energies of polysulfides show that Co^{3+}_{oh} sites have higher adsorption energy for sulfur active species (Figure 5e and Table S5). Typically, for transition metals, the d orbitals split to form an electron–filled lower Hubbard band (LHB) and an empty upper Hubbard band (UHB), referred to as the Mott–Hubbard splitting.[79, 82] Furthermore, the Coulombic interaction (U) between the d orbitals is inversely proportional to the orbital

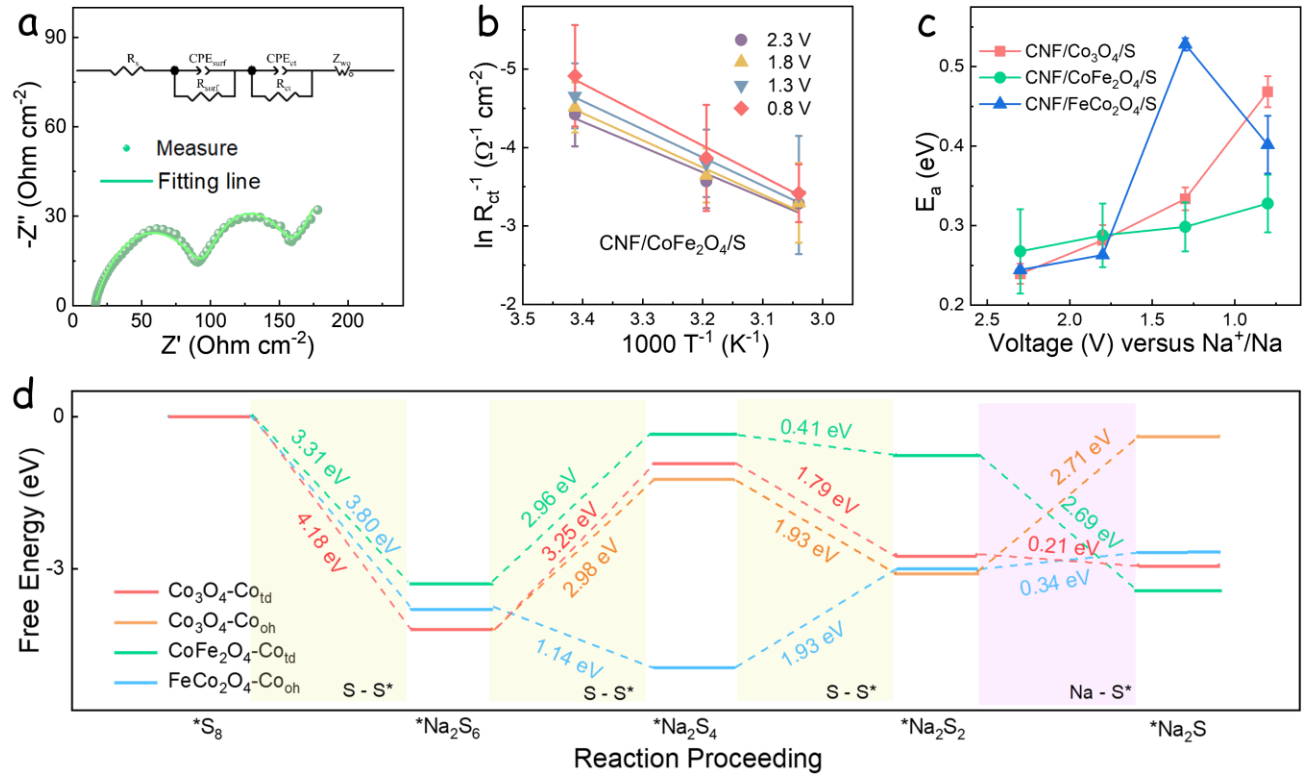

Figure 4. (a) Measured and fitted curves of the CNF/$CoFe_2O_4$/S electrode in half cell configuration. The measured EIS curves can be fitted with the equivalent circuit shown in the inset, where R_{surf} describes the deposition of adsorbed sodium polysulfide on the electrode surface, R_{ct} is attributed to the charge transfer process, and the tail line represents the Warburg revolt. (b) R_{ct} Arrhenius plot of CNF/$CoFe_2O_4$/S. The value of R_{ct} was obtained by fitting using an equivalent circuit, as shown in the inset of a. Error bars represent relative error in fitting R_{ct} values. (c) Activation energies of three sulfur electrodes at different voltages. The error comes from the linear fit of the Arrhenius plot of R_{ct}. (d) Relative energy distribution of various reacting species along the reaction pathway, SRR process in Co_3O_4–Co_{td}^{2+} (Co_{td}^{2+} as active site), Co_3O_4–Co_{oh}^{3+} (Co_{oh}^{3+} as active site), $CoFe_2O_4$ and $FeCo_2O_4$.

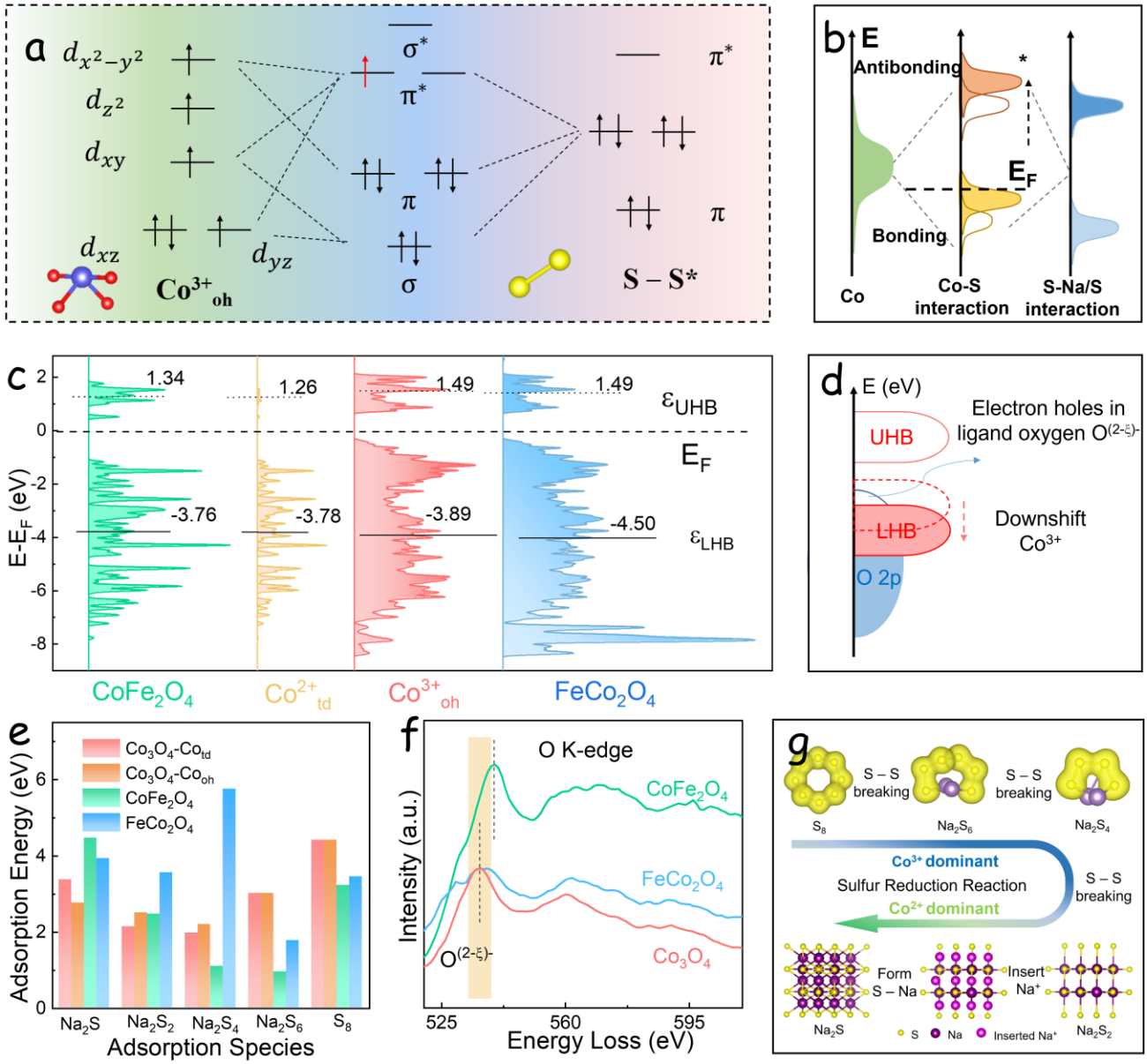

Figure 5. (a) Schematic representation of the favorable interaction between the S–S* intermediate and the 3d orbital of the Co^{3+}_{oh} site. (b) Schematic diagram of the chemical bond formation between the reactive surface and S–S or S–Na bond. (c) Calculated 3d orbital PDOS maps of local Co locations in various spinel models, and the associated band centers. (d) Chemical representation of activated oxygen ligands induced by Co^{3+} in the Mott–Hubbard model. (e) Adsorption energy between sulfur species and slab. (f) O K–edge EELS of various catalysts. (g) Schematic diagram of sulfur species conversion process.

size and strongly depends on the metal's valence state.[83] Compared to Co^{2+}_{td}, the orbital size of Co^{3+}_{oh} is reduced, resulting in an increased U value that enlarges the d–orbital splitting and downshifts the LHB to penetrate the p–orbital of the coordinated oxygen. This allows electrons to escape from the p–orbital of the ligand oxygen, creating localized holes, represented by $O^{(2-\delta)-}$ (Figure 5c). As shown in Figure 5d, the calculated d–band centers (ε_d) below and above the Fermi level (E_F) can be described as LHB–band centers (ε_{LHB}) and UHB–band centers (ε_{UHB}), respectively. We can verify quantitatively that the ε_{LHB} of Co^{3+}_{oh} in $FeCo_2O_4$ is much lower than that of Co^{2+}_{td} in $CoFe_2O_4$, which promotes the formation of $O^{(2-\delta)-}$. The existence of $O^{(2-\delta)-}$ could provide more electron holes and increase the adsorption between sulfur species and Co^{3+}_{oh}.

To further verify our hypotheses, we characterized the electronic structure of surface–coordinated oxygen using O K–edge EELS spectra. As depicted in Figure 5f, Co_3O_4 and $FeCo_2O_4$ exhibit a peak around 529 eV before the front–edge absorption. The shift of the peaks of Co_3O_4 and $FeCo_2O_4$ can be explained by the existence of localized holes in the ligand oxygen, which is consistent with the results of the Mott–Hubbard split theory analysis.[84] The PDOS of Co_{oh} with O 2p shows larger overlapping than Co_{td} (Figure S48). This indicates that electrons can be transferred from the p–band of the ligand oxygen to create $O^{(2-\delta)-}$, thereby reducing the electron–donating ability of ligand oxygen and enhancing the adsorption energy of active species on Co^{3+}_{oh}. The Co L–edge EELS could also prove the existence of $O^{(2-\delta)-}$. As shown in Figure S49, each spectrum contains two distinct peaks, corresponding to higher

energy L_2 and lower energy L_3, which can be attributed to the spin-orbit splitting of the 2p nuclear state.[85] Compared with Co_3O_4, the light energy of the Co L-edge spectrum of $CoFe_2O_4$ has a negative shift, which further indicates that the orbital space overlap of Co^{3+} and O is stronger than that of Co^{2+} and O.

3. CONCLUSION

In this study, the roles of octahedral and tetrahedral metal atoms in spinel catalysts of sodium polysulfide conversion were analyzed. Co^{3+}_{oh} and Co^{2+}_{td} in Co_3O_4 were in large part replaced by Fe ions to produce $FeCo_2O_4$ and $CoFe_2O_4$. A thorough characterization of the materials and their electrochemical properties using galvanostatic electrodeposition, activation energy calculated by the Arrhenius equation, and DFT calculations were carried out to quantify the difference between the SRR process of Co^{3+}_{oh} and Co^{2+}_{td}. The results show that Co^{3+}_{oh} is the main active center for the decomposition of sulfur–sulfur bonds, while Co^{2+}_{td} is the active center for the formation of Na–S bonds. This study comprehensively describes the geometric configuration dependence of spinel catalysts in the SRR process and expands on the general bimetallic synergistic "catalysis–adsorption" concept. The proposed idea of geometric configuration–mediated co–regulation can be applied to other catalytic reactions beyond SRRs, especially those involving complex intermediate behaviors at multiple active sites.

ASSOCIATED CONTENT

Supporting Information. The Supporting Information is available free of charge at

Experimental section; additional electrochemical measurements; material characterizations; and theoretical calculations (PDF).

AUTHOR INFORMATION

Corresponding Authors

Andreu Cabot − Catalonia Institute for Energy Research – IREC, Sant Adrià de Besòs, Barcelona 08930, Spain; ICREA, Pg. Lluís Companys 23, 08010 Barcelona, Spain; Email: acabot@irec.cat

Jin Yuan Zhou − Key Laboratory for Magnetism and Magnetic Materials of the Ministry of Education & School of Physical Science & Technology, Lanzhou University, Lanzhou, 730000, China; School of Physics and Electronic Information Engineering, Qinghai Normal University, Xining, 810008, China; Email: zhoujy@lzu.edu.cn

Xu Han − Catalan Institute of Nanoscience and Nanotechnology (ICN2), Campus UAB, 08193 Bellaterra, Barcelona, Catalonia, Spain. E–mail: xu.han@icn2.cat;

Authors

Chao Yue Zhang − Key Laboratory for Magnetism and Magnetic Materials of the Ministry of Education & School of Physical Science & Technology, Lanzhou University, Lanzhou, 730000, China; Catalonia Institute for Energy Research – IREC, Sant Adrià de Besòs, Barcelona 08930, Spain.

Xuan Lu – Catalonia Institute for Energy Research – IREC, Sant Adrià de Besòs, Barcelona 08930, Spain.

Jing Yu – Catalonia Institute for Energy Research – IREC, Sant Adrià de Besòs, Barcelona 08930, Spain; Catalan Institute of Nanoscience and Nanotechnology (ICN2), Campus UAB, 08193 Bellaterra, Barcelona, Catalonia, Spain.

Chaoqi Zhang – Catalonia Institute for Energy Research – IREC, Sant Adrià de Besòs, Barcelona 08930, Spain.

Chen Huang – Catalonia Institute for Energy Research – IREC, Sant Adrià de Besòs, Barcelona 08930, Spain.

Lluís Balcells – Institut de Ciència de Materials de Barcelona, ICMAB-CSIC, Campus de la UAB, 08193 Bellaterra, Catalonia, Spain.

Alba Garzón Manjón – Catalan Institute of Nanoscience and Nanotechnology (ICN2), Campus UAB, 08193 Bellaterra , Barcelona, Catalonia, Spain.

Jordi Jacas Biendicho – Catalonia Institute for Energy Research – IREC, Sant Adrià de Besòs, Barcelona 08930, Spain.

Junshan Li − K Institute of Advanced Study, Chengdu University, Chengdu, 610106 China.

Jordi Arbiol − Catalonia Institute for Energy Research – IREC, Sant Adrià de Besòs, Barcelona 08930, Spain; ICREA, Pg. Lluís Companys 23, 08010 Barcelona, Spain.

Gengzhi Sun − Key Laboratory of Flexible Electronics & Institute of Advanced Materials, Nanjing Tech University, 30 South Puzhu Road, Nanjing 211816, China.

Author Contributions

The manuscript was written through the contributions of all authors. All authors have approved the final version of the manuscript.

Funding Sources

This work was supported by the Innovation fund for small and medium–sized Enterprises in Gansu Province (No.22CX3JA006), Lanzhou Talent Innovation and Entrepreneurship Project (No.2022–2–81), National Natural Science Foundation of China (Grant Nos. 61801200) and partially by the Fundamental Research Funds for the Central Universities (Grant Nos.: lzujbky−2021−it33). J. S. Li thanks financial support from the Natural Science Foundation of Sichuan province (2022NSFSC1229). ICN2 acknowledges funding from Generalitat de Catalunya 2021SGR00457. This study is part of the Advanced Materials programme and was supported by MCIN with funding from European Union NextGenerationEU (PRTR-C17.I1) and by Generalitat de Catalunya. The authors thank the support from the project NANOGEN (PID2020-116093RB-C43), funded by MCIN/ AEI/10.13039/501100011033/ and by "ERDF A way of making Europe", by the "European Union". ICN2 is supported by the Severo Ochoa program from Spanish MCIN / AEI (Grant No.: CEX2021-001214-S) and is funded by the CERCA Programme / Generalitat de Catalunya. AGM has received funding from Grant RYC2021-033479-I funded by MCIN/AEI/ 10.13039/501100011033 and by European Union NextGenerationEU/PRTR. L. Balcells thanks the Ministry of Science and Innovation of Spain through the OXISHOT project (PID2021-128410OB-I00).

Notes

The authors declare no competing financial interest.

ACKNOWLEDGMENT

C. Y. Zhang, X. Lu, J. Yu, and C. Huang thank the China Scholarship Council for the scholarship support. The authors also greatly acknowledge the support supported by the Supercomputing Center of Lanzhou University, China. The

authors acknowledge the use of instrumentation as well as the technical advice provided by JEMCA at National Facility ALBA-CELLS ICTS. ICN2 acknowledges funding from "ERDF A way of making Europe", by the "European Union" and Generalitat de Catalunya for the project METCAM-FIB. Part of the present work has been performed in the framework of Universitat Autònoma de Barcelona Materials Science PhD program.

REFERENCES

(1) Zhang, C. Y.; Zhang, C.; Sun, G. W.; Pan, J. L.; Gong, L.; Sun, G. Z.; Biendicho, J. J.; Balcells, L.; Fan, X. L.; Morante, J. R.; Zhou, J. Y.; Cabot, A., Spin Effect to Promote Reaction Kinetics and Overall Performance of Lithium-Sulfur Batteries under External Magnetic Field. *Angew. Chem. Int. Ed.* **2022,** *61* (49), e202211570.

(2) Ye, C.; Jin, H.; Shan, J.; Jiao, Y.; Li, H.; Gu, Q.; Davey, K.; Wang, H.; Qiao, S.-Z., A Mo_5N_6 electrocatalyst for efficient Na_2S electrodeposition in room-temperature sodium-sulfur batteries. *Nat. Commun.* **2021,** *12* (1), 7195.

(3) Ye, C.; Shan, J.; Chao, D.; Liang, P.; Jiao, Y.; Hao, J.; Gu, Q.; Davey, K.; Wang, H.; Qiao, S.-Z., Catalytic Oxidation of K_2S via Atomic Co and Pyridinic N Synergy in Potassium–Sulfur Batteries. *J. Am. Chem. Soc.* **2021,** *143* (41), 16902-16907.

(4) Zhang, C. Y.; Gong, L.; Zhang, C.; Cheng, X.; Balcells, L.; Zeng, G.; Biendicho, J. J.; Li, J.; Sun, G. Z.; Zhou, J. Y.; Cabot, A., Sodium-Sulfur Batteries with Unprecedented Capacity, Cycling Stability and Operation Temperature Range Enabled by a $CoFe_2O_4$ Catalytic Additive Under an External Magnetic Field. *Adv. Funct. Mater.* **2023**, 2305908.

(5) Hao, H.; Hutter, T.; Boyce, B. L.; Watt, J.; Liu, P.; Mitlin, D., Review of Multifunctional Separators: Stabilizing the Cathode and the Anode for Alkali (Li, Na, and K) Metal–Sulfur and Selenium Batteries. *Chem. Rev.* **2022,** *122* (9), 8053-8125.

(6) Yang, D.; Liang, Z.; Tang, P.; Zhang, C.; Tang, M.; Li, Q.; Biendicho, J. J.; Li, J.; Heggen, M.; Dunin-Borkowski, R. E.; Xu, M.; Llorca, J.; Arbiol, J.; Morante, J. R.; Chou, S.-L.; Cabot, A., A High Conductivity 1D π–d Conjugated Metal–Organic Framework with Efficient Polysulfide Trapping-Diffusion-Catalysis in Lithium–Sulfur Batteries. *Adv. Mater.* **2022,** *34* (10), 2108835.

(7) Li, M.; Yang, D.; Biendicho, J. J.; Han, X.; Zhang, C.; Liu, K.; Diao, J.; Li, J.; Wang, J.; Heggen, M.; Dunin-Borkowski, R. E.; Wang, J.; Henkelman, G.; Morante, J. R.; Arbiol, J.; Chou, S.-L.; Cabot, A., Enhanced Polysulfide Conversion with Highly Conductive and Electrocatalytic Iodine-Doped Bismuth Selenide Nanosheets in Lithium–Sulfur Batteries. *Adv. Funct. Mater.* **2022,** *32* (26), 2200529.

(8) Zhang, C.; Fei, B.; Yang, D.; Zhan, H.; Wang, J.; Diao, J.; Li, J.; Henkelman, G.; Cai, D.; Biendicho, J. J.; Morante, J. R.; Cabot, A., Robust Lithium–Sulfur Batteries Enabled by Highly Conductive WSe_2-Based Superlattices with Tunable Interlayer Space. *Adv. Funct. Mater.* **2022,** *32* (24), 2201322.

(9) Zhang, C. Y.; Sun, G. W.; De Shi, Z.; Liu, Q. Y.; Pan, J. L.; Wang, Y. C.; Zhao, H.; Sun, G. Z.; Gao, X. P.; Pan, X. J.; Zhou, J. Y., Deciphering the catalysis essence of vanadium self-intercalated two-dimensional vanadium sulfides (V_5S_8) on lithium polysulfide towards high-rate and ultra-stable Li-S batteries. *Energy Stor. Mater.* **2021,** *43*, 471-481.

(10) Li, H.; Chen, C.; Yan, Y.; Yan, T.; Cheng, C.; Sun, D.; Zhang, L., Utilizing the Built-in Electric Field of p–n Junctions to Spatially Propel the Stepwise Polysulfide Conversion in Lithium–Sulfur Batteries. *Adv. Mater.* **2021,** *33* (51), 2105067.

(11) Huang, C.; Yu, J.; Li, C.; Cui, Z.; Zhang, C.; Zhang, C.; Nan, B.; Li, J.; Arbiol, J.; Cabot, A., Combined Defect and Heterojunction Engineering in ZnTe/$CoTe_2$@NC Sulfur Hosts Toward Robust Lithium–Sulfur Batteries. *Adv. Funct. Mater.* **2023**, 2305624.

(12) Yang, D.; Li, M.; Zheng, X.; Han, X.; Zhang, C.; Jacas Biendicho, J.; Llorca, J.; Wang, J.; Hao, H.; Li, J.; Henkelman, G.; Arbiol, J.; Morante, J. R.; Mitlin, D.; Chou, S.; Cabot, A., Phase Engineering of Defective Copper Selenide toward Robust Lithium–Sulfur Batteries. *ACS Nano* **2022,** *16* (7), 11102-11114.

(13) Wu, J.; Wang, X.; Zheng, W.; Sun, Y.; Xie, Y.; Ma, K.; Zhang, Z.; Liao, Q.; Tian, Z.; Kang, Z.; Zhang, Y., Identifying and Interpreting Geometric Configuration-Dependent Activity of Spinel Catalysts for Water Reduction. *J. Am. Chem. Soc.* **2022,** *144* (41), 19163-19172.

(14) Luo, Z.; Irtem, E.; Ibáñez, M.; Nafria, R.; Martí-Sánchez, S.; Genç, A.; de la Mata, M.; Liu, Y.; Cadavid, D.; Llorca, J.; Arbiol, J.; Andreu, T.; Morante, J. R.; Cabot, A., Mn_3O_4@$CoMn_2O_4$–Co_xO_y Nanoparticles: Partial Cation Exchange Synthesis and Electrocatalytic Properties toward the Oxygen Reduction and Evolution Reactions. *ACS Appl. Mater. Interfaces* **2016,** *8* (27), 17435-17444.

(15) Urbain, F.; Du, R.; Tang, P.; Smirnov, V.; Andreu, T.; Finger, F.; Jimenez Divins, N.; Llorca, J.; Arbiol, J.; Cabot, A.; Morante, J. R., Upscaling high activity oxygen evolution catalysts based on $CoFe_2O_4$ nanoparticles supported on nickel foam for power-to-gas electrochemical conversion with energy efficiencies above 80%. *Appl. Catal. B* **2019,** *259*, 118055.

(16) Dey, S.; Dhal, G. C., Catalytic conversion of carbon monoxide into carbon dioxide over spinel catalysts: An overview. *Mater. Sci. Technol.* **2019,** *2* (3), 575-588.

(17) Advani, J. H.; More, G. S.; Srivastava, R., Spinel-based catalysts for the biomass valorisation of platform molecules via oxidative and reductive transformations. *Green Chem.* **2022,** *24* (9), 3574-3604.

(18) Zhou, X.; Jia, Z.; Zhang, X.; Wang, B.; Liu, X.; Xu, B.; Bi, L.; Wu, G., Electromagnetic wave absorption performance of $NiCo_2X_4$ (X = O, S, Se, Te) spinel structures. *Chem. Eng. J.* **2021,** *420*, 129907.

(19) He, Y.; Bi, M.; Yu, H.; Zhang, C.; Majeed, A.; Shen, X.; Yao, S., Nanoscale $CuFe_2O_4$ Uniformly Decorated on Nitrogen-Doped Carbon Nanofibers as Highly Efficient Catalysts for Polysulfide Conversion in Lithium-Sulfur Batteries. *ChemElectroChem* **2021,** *8* (23), 4564-4572.

(20) Park, S.; Lee, Y. H.; Choi, S.; Seo, H.; Lee, M. Y.; Balamurugan, M.; Nam, K. T., Manganese oxide-based heterogeneous electrocatalysts for water oxidation. *Energy Environ. Sci.* **2020,** *13* (8), 2310-2340.

(21) Wang, Z.; Wu, P.; Zou, X.; Wang, S.; Du, L.; Ouyang, T.; Liu, Z.-Q., Optimizing the Oxygen-Catalytic Performance of Zn–Mn–Co Spinel by Regulating the Bond Competition at Octahedral Sites. *Adv. Funct. Mater.* **2023,** *33* (16), 2214275.

(22) Zhang, C.; Biendicho, J. J.; Zhang, T.; Du, R.; Li, J.; Yang, X.; Arbiol, J.; Zhou, Y.; Morante, J. R.; Cabot, A., Combined High Catalytic Activity and Efficient Polar Tubular Nanostructure in Urchin-Like Metallic $NiCo_2Se_4$ for High-Performance Lithium–Sulfur Batteries. *Adv. Funct. Mater.* **2019,** *29* (34), 1903842.

(23) Hu, S.; Yi, M.; Wu, H.; Wang, T.; Ma, X.; Liu, X.; Zhang, J., Ionic-Liquid-Assisted Synthesis of N, F, and B Co-Doped $CoFe_2O_{4-x}$ on Multiwalled Carbon Nanotubes with Enriched Oxygen Vacancies for Li–S Batteries. *Adv. Funct. Mater.* **2022,** *32* (14), 2111084.

(24) Liu, Y.-T.; Han, D.-D.; Wang, L.; Li, G.-R.; Liu, S.; Gao, X.-P., $NiCo_2O_4$ Nanofibers as Carbon-Free Sulfur Immobilizer to Fabricate Sulfur-Based Composite with High Volumetric Capacity for Lithium–Sulfur Battery. *Adv. Energy Mater.* **2019,** *9* (11), 1803477.

(25) Luo, D.; Li, G.; Deng, Y.-P.; Zhang, Z.; Li, J.; Liang, R.; Li, M.; Jiang, Y.; Zhang, W.; Liu, Y.; Lei, W.; Yu, A.; Chen, Z., Synergistic Engineering of Defects and Architecture in Binary Metal Chalcogenide toward Fast and Reliable Lithium–Sulfur Batteries. *Adv. Energy Mater.* **2019,** *9* (18), 1900228.

(26) Raulo, A.; Singh, S.; Gupta, A.; Srivastava, R.; Nandan, B., Metal oxide heterostructure decorated carbon nanofiber as a novel

redox catalyst for high performance Lithium-Sulfur batteries. *Appl. Surf. Sci.* **2021,** *569*, 151054.
(27) Mao, Y.; Chen, D.; Chen, Y.; Xiao, Y.; Li, T.; Hao, X.; You, J.; Wang, W.; Li, Y.; Meng, S.; Wu, J.; Zhao, J., Construction of composite separator with 3D hierarchical spinel structure in Lithium-Sulfur batteries. *Chem. Eng. J.* **2022,** *448*, 137766.
(28) Zhu, Y.; Zuo, Y.; Ye, F.; Zhou, J.; Tang, Y.; Chen, Y., Dual-regulation strategy to enhance electrochemical catalysis ability of $NiCo_2O_{4-x}$ for polysulfides conversion in Li-S batteries. *Chem. Eng. J.* **2022,** *428*, 131109.
(29) Tian, L.; Zhang, Z.; Liu, S.; Li, G.; Gao, X., High-Entropy Spinel Oxide Nanofibers as Catalytic Sulfur Hosts Promise the High Gravimetric and Volumetric Capacities for Lithium–Sulfur Batteries. *Energy Environ. Mater.* **2022,** *5* (2), 645-654.
(30) Li, H.; Shi, P.; Wang, L.; Yan, T.; Guo, T.; Xia, X.; Chen, C.; Mao, J.; Sun, D.; Zhang, L., Cooperative Catalysis of Polysulfides in Lithium-Sulfur Batteries through Adsorption Competition by Tuning Cationic Geometric Configuration of Dual-active Sites in Spinel Oxides. *Angew. Chem. Int. Ed.* **2023,** *62* (8), e202216286.
(31) Zhang, C.; Du, R.; Biendicho, J. J.; Yi, M.; Xiao, K.; Yang, D.; Zhang, T.; Wang, X.; Arbiol, J.; Llorca, J.; Zhou, Y.; Morante, J. R.; Cabot, A., Tubular CoFeP@CN as a Mott–Schottky Catalyst with Multiple Adsorption Sites for Robust Lithium−Sulfur Batteries. *Adv. Energy Mater.* **2021,** *11* (24), 2100432.
(32) Zhang, C. Y.; Zhang, C.; Pan, J. L.; Sun, G. W.; Shi, Z.; Li, C.; Chang, X.; Sun, G. Z.; Zhou, J. Y.; Cabot, A., Surface strain-enhanced MoS_2 as a high-performance cathode catalyst for lithium–sulfur batteries. *eScience* **2022,** *2* (4), 405-415.
(33) Zhang, C. Y.; Lu, Z. W.; Wang, Y. H.; Dai, Z.; Zhao, H.; Sun, G. Z.; Lan, W.; Pan, X. J.; Zhou, J. Y.; Xie, E. Q., Cooperative chemisorption of polysulfides via 2D hexagonal WS_2-rimmed Co_9S_8 heterostructures for lithium–sulfur batteries. *Chem. Eng. J.* **2020,** *392*, 123734.
(34) Du, Z.; Chen, X.; Hu, W.; Chuang, C.; Xie, S.; Hu, A.; Yan, W.; Kong, X.; Wu, X.; Ji, H.; Wan, L.-J., Cobalt in Nitrogen-Doped Graphene as Single-Atom Catalyst for High-Sulfur Content Lithium–Sulfur Batteries. *J. Am. Chem. Soc.* **2019,** *141* (9), 3977-3985.
(35) Wen, Y.; Shen, Z.; Hui, J.; Zhang, H.; Zhu, Q., Co/CoSe Junctions Enable Efficient and Durable Electrocatalytic Conversion of Polysulfides for High-Performance Li–S Batteries. *Adv. Energy Mater.* **2023,** *13* (20), 2204345.
(36) Hung, S.-F.; Hsu, Y.-Y.; Chang, C.-J.; Hsu, C.-S.; Suen, N.-T.; Chan, T.-S.; Chen, H. M., Unraveling Geometrical Site Confinement in Highly Efficient Iron-Doped Electrocatalysts toward Oxygen Evolution Reaction. *Adv. Energy Mater.* **2018,** *8* (7), 1701686.
(37) Hou, Y. H.; Zhao, Y. J.; Liu, Z. W.; Yu, H. Y.; Zhong, X. C.; Qiu, W. Q.; Zeng, D. C.; Wen, L. S., Structural, electronic and magnetic properties of partially inverse spinel $CoFe_2O_4$: a first-principles study. *J. Phys. D* **2010,** *43* (44), 445003.
(38) Burns, R. G.; Fyfe, W. S., Site of Preference Energy and Selective Uptake of Transition-Metal Ions from a Magma. *Science* **1964,** *144* (3621), 1001-1003.
(39) Liu, Y.; Ying, Y.; Fei, L.; Liu, Y.; Hu, Q.; Zhang, G.; Pang, S. Y.; Lu, W.; Mak, C. L.; Luo, X.; Zhou, L.; Wei, M.; Huang, H., Valence Engineering via Selective Atomic Substitution on Tetrahedral Sites in Spinel Oxide for Highly Enhanced Oxygen Evolution Catalysis. *J. Am. Chem. Soc.* **2019,** *141* (20), 8136-8145.
(40) Wu, T.; Ren, X.; Sun, Y.; Sun, S.; Xian, G.; Scherer, G. G.; Fisher, A. C.; Mandler, D.; Ager, J. W.; Grimaud, A.; Wang, J.; Shen, C.; Yang, H.; Gracia, J.; Gao, H.-J.; Xu, Z. J., Spin pinning effect to reconstructed oxyhydroxide layer on ferromagnetic oxides for enhanced water oxidation. *Nat. Commun.* **2021,** *12* (1), 3634.
(41) Ren, X.; Wu, T.; Sun, Y.; Li, Y.; Xian, G.; Liu, X.; Shen, C.; Gracia, J.; Gao, H.-J.; Yang, H.; Xu, Z. J., Spin-polarized oxygen evolution reaction under magnetic field. *Nat. Commun.* **2021,** *12* (1), 2608.
(42) Zhou, Z.; Zhang, Y.; Wang, Z.; Wei, W.; Tang, W.; Shi, J.; Xiong, R., Electronic structure studies of the spinel $CoFe_2O_4$ by X-ray photoelectron spectroscopy. *Appl. Surf. Sci.* **2008,** *254* (21), 6972-6975.
(43) Bhargava, A.; Eppstein, R.; Sun, J.; Smeaton, M. A.; Paik, H.; Kourkoutis, L. F.; Schlom, D. G.; Caspary Toroker, M.; Robinson, R. D., Breakdown of the Small-Polaron Hopping Model in Higher-Order Spinels. *Adv. Mater.* **2020,** *32* (49), 2004490.
(44) Wei, C.; Feng, Z.; Scherer, G. G.; Barber, J.; Shao-Horn, Y.; Xu, Z. J., Cations in Octahedral Sites: A Descriptor for Oxygen Electrocatalysis on Transition-Metal Spinels. *Adv. Mater.* **2017,** *29* (23), 1606800.
(45) Bhargava, A.; Chen, C. Y.; Dhaka, K.; Yao, Y.; Nelson, A.; Finkelstein, K. D.; Pollock, C. J.; Caspary Toroker, M.; Robinson, R. D., Mn Cations Control Electronic Transport in Spinel $Co_xMn_{3-x}O_4$ Nanoparticles. *Chem. Mater.* **2019,** *31* (11), 4228-4233.
(46) Sanchez-Lievanos, K. R.; Stair, J. L.; Knowles, K. E., Cation Distribution in Spinel Ferrite Nanocrystals: Characterization, Impact on their Physical Properties, and Opportunities for Synthetic Control. *Inorg. Chem.* **2021,** *60* (7), 4291-4305.
(47) Zhu, J.; Du, Q.; Arif Khan, M.; Zhao, H.; Fang, J.; Ye, D.; Zhang, J., 2D porous Co-Mo nitride heterostructures nanosheets for highly effective electrochemical water splitting. *Appl. Surf. Sci.* **2023,** *623*, 156989.
(48) Liu, S.; Liu, X.; Chen, M.; Wang, D.; Ge, X.; Zhang, W.; Wang, X.; Wang, C.; Qin, T.; Qin, H.; Qiao, L.; Zhang, D.; Ou, X.; Zheng, W., High-density/efficient surface active sites on modified separators to boost Li-S batteries via atomic Co^{3+}-Se termination. *Nano Res.* **2022,** *15* (8), 7199-7208.
(49) Wang, X.; Li, J.; Xue, Q.; Han, X.; Xing, C.; Liang, Z.; Guardia, P.; Zuo, Y.; Du, R.; Balcells, L.; Arbiol, J.; Llorca, J.; Qi, X.; Cabot, A., Sulfate-Decorated Amorphous–Crystalline Cobalt-Iron Oxide Nanosheets to Enhance O–O Coupling in the Oxygen Evolution Reaction. *ACS Nano* **2023,** *17* (1), 825-836.
(50) Wang, X.; Han, X.; Du, R.; Liang, Z.; Zuo, Y.; Guardia, P.; Li, J.; Llorca, J.; Arbiol, J.; Zheng, R.; Cabot, A., Unveiling the role of counter-anions in amorphous transition metal-based oxygen evolution electrocatalysts. *Appl. Catal. B* **2023,** *320*, 121988.
(51) Wang, X.; Han, X.; Du, R.; Xing, C.; Qi, X.; Liang, Z.; Guardia, P.; Arbiol, J.; Cabot, A.; Li, J., Cobalt Molybdenum Nitride-Based Nanosheets for Seawater Splitting. *ACS Appl. Mater. Interfaces* **2022,** *14* (37), 41924-41933.
(52) He, R.; Yang, L.; Zhang, Y.; Wang, X.; Lee, S.; Zhang, T.; Li, L.; Liang, Z.; Chen, J.; Li, J.; Ostovari Moghaddam, A.; Llorca, J.; Ibáñez, M.; Arbiol, J.; Xu, Y.; Cabot, A., A CrMnFeCoNi high entropy alloy boosting oxygen evolution/reduction reactions and zinc-air battery performance. *Energy Stor. Mater.* **2023,** *58*, 287-298.
(53) Jiang, S.; Chen, F.; Zhu, L.; Yang, Z.; Lin, Y.; Xu, Q.; Wang, Y., Insight into the Catalytic Activity of Amorphous Multimetallic Catalysts under a Magnetic Field toward the Oxygen Evolution Reaction. *ACS Appl. Mater. Interfaces* **2022,** *14* (8), 10227-10236.
(54) McIntyre, N. S.; Cook, M. G., X-ray photoelectron studies on some oxides and hydroxides of cobalt, nickel, and copper. *Anal. Chem.* **1975,** *47* (13), 2208-2213.
(55) Huang, C.; Gao, A.; Yi, F.; Wang, Y.; Shu, D.; Liang, Y.; Zhu, Z.; Ling, J.; Hao, J., Metal organic framework derived hollow NiS@C with S-vacancies to boost high-performance supercapacitors. *Chem. Eng. J.* **2021,** *419*, 129643.
(56) Zhang, Z.; Li, J.; Qian, J.; Li, Z.; Jia, L.; Gao, D.; Xue, D., Significant Change of Metal Cations in Geometric Sites by Magnetic-Field Annealing $FeCo_2O_4$ for Enhanced Oxygen Catalytic Activity. *Small* **2022,** *18* (7), 2104248.
(57) Verma, S.; Joy, P. A.; Kurian, S., Structural, magnetic and Mössbauer spectral studies of nanocrystalline $Ni_{0.5}Zn_{0.5}Fe_2O_4$ ferrite powders. *J. Alloys Compd.* **2011,** *509* (37), 8999-9004.
(58) Liao, Y. Y.; Li, Y. W.; Hu, Z. G.; Chu, J. H., Temperature dependent phonon Raman scattering of highly a-axis oriented

$CoFe_2O_4$ inverse spinel ferromagnetic films grown by pulsed laser deposition. *Appl. Phys. Lett.* **2012,** *100* (7), 071905.

(59) Sun, S.; Sun, Y.; Zhou, Y.; Xi, S.; Ren, X.; Huang, B.; Liao, H.; Wang, L. P.; Du, Y.; Xu, Z. J., Shifting Oxygen Charge Towards Octahedral Metal: A Way to Promote Water Oxidation on Cobalt Spinel Oxides. *Angew. Chem. Int. Ed.* **2019,** *58* (18), 6042-6047.

(60) Zhang, Y.; Kang, C.; Zhao, W.; Song, Y.; Zhu, J.; Huo, H.; Ma, Y.; Du, C.; Zuo, P.; Lou, S.; Yin, G., d-p Hybridization-Induced "Trapping–Coupling–Conversion" Enables High-Efficiency Nb Single-Atom Catalysis for Li–S Batteries. *J. Am. Chem. Soc.* **2023,** *145* (3), 1728-1739.

(61) Zhang, B.-W.; Sheng, T.; Liu, Y.-D.; Wang, Y.-X.; Zhang, L.; Lai, W.-H.; Wang, L.; Yang, J.; Gu, Q.-F.; Chou, S.-L.; Liu, H.-K.; Dou, S.-X., Atomic cobalt as an efficient electrocatalyst in sulfur cathodes for superior room-temperature sodium-sulfur batteries. *Nat. Commun.* **2018,** *9* (1), 4082.

(62) Wei, S.; Xu, S.; Agrawral, A.; Choudhury, S.; Lu, Y.; Tu, Z.; Ma, L.; Archer, L. A., A stable room-temperature sodium–sulfur battery. *Nat. Commun.* **2016,** *7* (1), 11722.

(63) Lei, Y.; Wu, C.; Lu, X.; Hua, W.; Li, S.; Liang, Y.; Liu, H.; Lai, W.-H.; Gu, Q.; Cai, X.; Wang, N.; Wang, Y.-X.; Chou, S.-L.; Liu, H.-K.; Wang, G.; Dou, S.-X., Streamline Sulfur Redox Reactions to Achieve Efficient Room-Temperature Sodium–Sulfur Batteries. *Angew. Chem. Int. Ed.* **2022,** *61* (16), e202200384.

(64) He, R.; Yang, L.; Zhang, Y.; Jiang, D.; Lee, S.; Horta, S.; Liang, Z.; Lu, X.; Moghaddam, A. O.; Li, J.; Ibáñez, M.; Xu, Y.; Zhou, Y.; Cabot, A., A 3d-4d-5d High Entropy Alloy as a Bifunctional Oxygen Catalyst for Robust Aqueous Zinc-Air Batteries. *Adv. Mater.* **2023**, 2303719.

(65) Xia, Z.; Guo, S., Strain engineering of metal-based nanomaterials for energy electrocatalysis. *Chem. Soc. Rev.* **2019,** *48* (12), 3265-3278.

(66) Miller, E. L.; Rocheleau, R. E., Electrochemical Behavior of Reactively Sputtered Iron ‐ Doped Nickel Oxide. *J. Electrochem. Soc.* **1997,** *144* (9), 3072.

(67) Plieth, W., *Electrochemistry for materials science*. Elsevier: 2008; p 195-203.

(68) Pei, A.; Zheng, G.; Shi, F.; Li, Y.; Cui, Y., Nanoscale Nucleation and Growth of Electrodeposited Lithium Metal. *Nano Lett.* **2017,** *17* (2), 1132-1139.

(69) Winand, R., Electrocrystallization: Fundamental considerations and application to high current density continuous steel sheet plating. *J. Appl. Electrochem.* **1991,** *21* (5), 377-385.

(70) Milchev, A.; Irene Montenegro, M., A galvanostatic study of electrochemical nucleation. *J. Electroanal. Chem.* **1992,** *333* (1), 93-102.

(71) Oxtoby, D. W.; Kashchiev, D., A general relation between the nucleation work and the size of the nucleus in multicomponent nucleation. *J. Chem. Phys.* **1994,** *100* (10), 7665-7671.

(72) Valov, I.; Sapezanskaia, I.; Nayak, A.; Tsuruoka, T.; Bredow, T.; Hasegawa, T.; Staikov, G.; Aono, M.; Waser, R., Atomically controlled electrochemical nucleation at superionic solid electrolyte surfaces. *Nat. Mater.* **2012,** *11* (6), 530-535.

(73) Peng, L.; Wei, Z.; Wan, C.; Li, J.; Chen, Z.; Zhu, D.; Baumann, D.; Liu, H.; Allen, C. S.; Xu, X.; Kirkland, A. I.; Shakir, I.; Almutairi, Z.; Tolbert, S.; Dunn, B.; Huang, Y.; Sautet, P.; Duan, X., A fundamental look at electrocatalytic sulfur reduction reaction. *Nat. Catal.* **2020,** *3* (9), 762-770.

(74) Li, J.; Li, L.; Ma, X.; Han, X.; Xing, C.; Qi, X.; He, R.; Arbiol, J.; Pan, H.; Zhao, J.; Deng, J.; Zhang, Y.; Yang, Y.; Cabot, A., Selective Ethylene Glycol Oxidation to Formate on Nickel Selenide with Simultaneous Evolution of Hydrogen. *Adv. Sci.* **2023,** *10* (15), 2300841.

(75) Dai, J.; Yang, C.; Xu, Y.; Wang, X.; Yang, S.; Li, D.; Luo, L.; Xia, L.; Li, J.; Qi, X.; Cabot, A.; Dai, L., MoS_2@Polyaniline for Aqueous Ammonium-Ion Supercapacitors. *Adv. Mater.* **2023**, 2303732.

(76) Chen, Y.; Qi, D.; Wang, H.; Xu, Z.; Yi, C.; Zhang, Z., Corrosion behavior of aluminum bronze under thin electrolyte layers containing artificial seawater. *Int. J. Electrochem. Sci.* **2015,** *10* (11), 9056-9072.

(77) Tan, G.; Xu, R.; Xing, Z.; Yuan, Y.; Lu, J.; Wen, J.; Liu, C.; Ma, L.; Zhan, C.; Liu, Q.; Wu, T.; Jian, Z.; Shahbazian-Yassar, R.; Ren, Y.; Miller, D. J.; Curtiss, L. A.; Ji, X.; Amine, K., Burning lithium in CS_2 for high-performing compact Li_2S–graphene nanocapsules for Li–S batteries. *Nat. Energy* **2017,** *2* (7), 17090.

(78) Li, Z.; Sami, I.; Yang, J.; Li, J.; Kumar, R. V.; Chhowalla, M., Lithiated metallic molybdenum disulfide nanosheets for high-performance lithium–sulfur batteries. *Nat. Energy* **2023,** *8* (1), 84-93.

(79) Assat, G.; Tarascon, J.-M., Fundamental understanding and practical challenges of anionic redox activity in Li-ion batteries. *Nat. Energy* **2018,** *3* (5), 373-386.

(80) Chen, H.; Wu, Z.; Zheng, M.; Liu, T.; Yan, C.; Lu, J.; Zhang, S., Catalytic materials for lithium-sulfur batteries: mechanisms, design strategies and future perspective. *Mater. Today* **2022,** *52*, 364-388.

(81) Steudel, R., Properties of Sulfur-Sulfur Bonds. *Angew. Chem. Int. Ed. Engl.* **1975,** *14* (10), 655-664.

(82) Huang, Z.-F.; Song, J.; Du, Y.; Xi, S.; Dou, S.; Nsanzimana, J. M. V.; Wang, C.; Xu, Z. J.; Wang, X., Chemical and structural origin of lattice oxygen oxidation in Co–Zn oxyhydroxide oxygen evolution electrocatalysts. *Nat. Energy* **2019,** *4* (4), 329-338.

(83) Zaanen, J.; Sawatzky, G. A.; Allen, J. W., Band gaps and electronic structure of transition-metal compounds. *Phys. Rev. Lett.* **1985,** *55* (4), 418-421.

(84) Zhang, N.; Feng, X.; Rao, D.; Deng, X.; Cai, L.; Qiu, B.; Long, R.; Xiong, Y.; Lu, Y.; Chai, Y., Lattice oxygen activation enabled by high-valence metal sites for enhanced water oxidation. *Nat. Commun.* **2020,** *11* (1), 4066.

(85) Brown, M.; Peierls, R. E.; Stern, E. A., White lines in x-ray absorption. *Phys. Rev. B* **1977,** *15* (2), 738-744.